

# Full-Sample X-ray Microcomputed Tomography Analysis of Supercritical CO<sub>2</sub> Fracturing in Tight Sandstone: Effect of Stress on Fracture Dynamics

Bing Yang, Haizhu Wang,\* Zhonghou Shen, Olufemi Olorode, Bin Wang, Yong Zheng, Wanjuan Yan, and Zhaoyang Jia

Cite This: *Energy Fuels* 2021, 35, 1308–1321

Read Online

ACCESS |

Metrics & More

Article Recommendations

**ABSTRACT:** The commercial production from tight oil and gas reservoirs has been facilitated by the multistage hydraulic fracturing of horizontal wells. This process typically requires the pumping of large amounts of slick water into the subsurface, and this could be challenging in areas with a limited supply of water. Despite the commercial success of hydraulic fracturing with water, it still faces the problem of clay swelling and potential contamination of underground water. This has led to research studies and field applications of liquid or supercritical carbon dioxide (SC-CO<sub>2</sub>) fracturing in unconventional oil and gas resources. Considering that the propagation and characteristics of these man-made fractures are controlled by the fracturing fluid and mechanical state of the reservoir, we performed a series of fracturing experiments on tight sandstones using water and SC-CO<sub>2</sub> at different stress magnitudes. To explore the morphology of the fractures and quantify their attributes, we proposed a novel full-sample fracture analysis approach, which is based on microcomputed tomography (CT) imaging. The results of this study indicate that the breakdown pressure is a linear function of the minimum principal stress and tensile strength. We observe that the pattern and geometry of the fractures created from SC-CO<sub>2</sub> fracturing is more complex than those of water fracturing under the same stress conditions. Our experimental results also indicate that smaller differential stresses lead to the creation of more fracture branches and that fracture propagation is significantly affected by the presence of initial bedding planes. Furthermore, our quantification of the fracture attributes (based on fracture extraction and digitization) indicates that SC-CO<sub>2</sub> fracturing leads to the creation of more complex fractures with rougher surfaces than water fracturing. This experimental study proposes a new full-sample fracture quantification approach, which can be implemented to analyze fracture attributes precisely and effectively. The results from this work could provide insights and guidance for the field application of SC-CO<sub>2</sub> fracturing in unconventional oil and gas resources.

## 1. INTRODUCTION

The significant decline in the production of conventional oil and gas reservoirs around the world has led to the commercial development of unconventional resources, such as tight sands. However, the efficient development of these resources still faces numerous challenges.<sup>1–3</sup> As of this writing, the commercial development of unconventional oil and gas reservoirs typically involves the multistage hydraulic fracturing of horizontal wells by injecting a mixture of water and chemical additives (known as slickwater) at high pressures.<sup>4</sup> This inevitably leads to problems such as clay swelling (in formations with clay minerals), environmental contamination, and formation damage, among others.<sup>5–7</sup> Therefore, various researchers have considered the use of other fracturing fluids that minimize formation damage and are more environmentally friendly. One of such potential fracturing fluids is supercritical CO<sub>2</sub> (SC-CO<sub>2</sub>), which is an anhydrous CO<sub>2</sub> that is obtained when the temperature and pressure exceed 31.1 °C and 7.38 MPa, respectively. Due to its special physical and chemical properties, SC-CO<sub>2</sub> has been considered as an alternative working fluid for the hydraulic fracturing of unconventional resources.<sup>8–12</sup> It is also well-known that SC-CO<sub>2</sub> fracturing can help to avoid clay swelling in the high-clay

reservoirs and minimizes the contamination of the surface environment and subsurface aquifers.<sup>13,14</sup> It is also applicable in arid regions where the supply of water is limited.<sup>15–17</sup> Consequently, the development of unconventional resources using SC-CO<sub>2</sub> is regarded as promising technology recently.<sup>18–21</sup>

Recently, a great number of simulation and experimental studies have been performed on SC-CO<sub>2</sub> fracturing. Several researchers have studied the effect of viscosity on the hydraulic fracturing mechanism. Ishida et al. (2004; 2012), Inui et al. (2014), Bennour et al. (2015), Li et al. (2016), Zhang et al. (2017), and Wang et al. (2018)<sup>22–28</sup> performed fracturing experiments and simulations with different fluids (such as oil, water, CO<sub>2</sub>, etc.) to investigate the fracturing characteristics. Their results indicated that fluids with lower viscosities create a

Received: October 23, 2020  
Revised: December 9, 2020  
Published: January 7, 2021



smaller formation breakdown pressure (FBP) than those with high viscosities. They also show that low-viscosity fracturing fluids (such as SC-CO<sub>2</sub>) tend to induce shear-dominant fractures, whereas viscous fluids are more likely to induce tensile-dominant fractures. On this basis, Zhang et al. (2020)<sup>29</sup> concluded that shear deformation can enhance the flow conductivity more than in cases without shear deformation. More recently, Zhou et al. (2016), Li et al. (2016), Jia et al. (2018), Li et al. (2019), and Yang et al. (2020)<sup>27,30–33</sup> conducted fracturing experiments to characterize the morphology and other attributes of these fractures. The results show that SC-CO<sub>2</sub> can induce more complex fracture geometries with a higher fracture surface roughness than in fractures generated by water fracturing. Additionally, Li et al. (2016) indicate that a positive relation may exist between the minimum principal stress and the formation breakdown pressure. The fracturing experiments (using water and SC-CO<sub>2</sub>) performed by Zhang et al. (2017), He et al. (2020), Zhao et al. (2018), and Hu et al. (2019)<sup>34–37</sup> suggest that the fracturing process is influenced not only by fluids but also by the bedding planes, pre-existing natural fractures, in situ stresses, etc.

It is inevitable that the stress loading (state) in the subsurface will have a significant impact on the fracture initiation and propagation. Even though several researchers have studied the effect of the in situ stress state on fracture initiation and propagation,<sup>26</sup> the study of the fracturing characteristics in rocks with different geomechanical properties still appears to be far from being conclusive. Therefore, in this work, we investigate the mechanical response and fracture propagation when the rock samples are applied to different stress states. Although several tools and fracture description methods (such as optical observation, AE monitoring, two-dimensional CT scanning, profilometry techniques, etc.) have been employed in previous studies to characterize fracture properties (such as the morphology, complexity, roughness, etc.),<sup>32,34,36–38</sup> these tools either lack measurement accuracy or cannot be applied on an entire core plug or sample.<sup>33</sup> To achieve a full-sample quantitative analysis of fracturing, we propose a more accurate and nondestructive method to investigate the fracture morphology.

In this study, we perform hydraulic fracturing experiments on tight sandstone samples (under the triaxial stress condition) using water and SC-CO<sub>2</sub>. We investigate the fracture characteristics of the sample, when subjected to various magnitudes and states of stress. We also applied a full-sample nonintrusive fracture analysis<sup>33</sup> (based on micro-CT scanning) to characterize the fracture morphology and quantitative attributes. This work facilitates an understanding of the effect of the magnitude and states of stress on fracture propagation during SC-CO<sub>2</sub> fracturing of tight sandstones. It could also lay a foundation for the field application of SC-CO<sub>2</sub> fracturing in tight sands and other unconventional resources.

## 2. EXPERIMENTAL METHODS

**2.1. Rock Sample Preparation.** To investigate the mechanical response and the fracture characteristics when hydraulic fracturing is performed in tight formations, representative tight sandstone outcrops were collected from the Yanchang oil field in China. Standard cylindrical core plugs or samples (with diameters and heights of 50 and 100 mm, respectively) were then cored from these outcrops in a direction perpendicular to the bedding plane. To mimic the conventional wellbore into which fracturing fluids are injected, we drilled a borehole with a diameter of 9 mm and a depth of 45 mm in

the center of the core sample. Furthermore, we attached a stainless-steel casing with a diameter of 8 mm and a depth of 35 mm to the borehole using epoxy resin adhesives. This left an open-hole section of 10 mm at the bottom of borehole.

Prior to the fracturing experiment, we performed a series of rock tests to determine the mechanical properties of the rock, such as uniaxial compressive strength and splitting tensile strength, among others. The mineral composition and natural structure of the samples were acquired using an X-ray diffractometer and casting slice analysis. The basic petrophysical properties of the rock sample is summarized in Table 1. Figure 1 presents a rock slice and composition analysis,

**Table 1. Basic Mechanical Properties of the Core Sample**

density (g/cm <sup>3</sup> )	2.67
compressive strength (MPa)	186.5
tensile strength (MPa)	5.27
elastic modulus (GPa)	13.4
poisson's ratio	0.246
permeability (10 <sup>-12</sup> m <sup>2</sup> )	0.057
porosity (%)	11.49

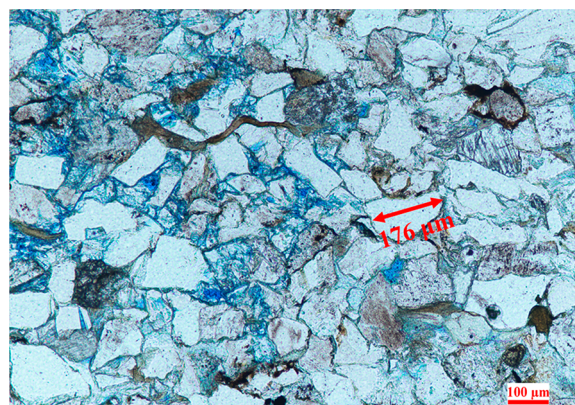


**Figure 1.** Rock slice and compositional analysis shows that the rock contains 68% quartz, 9% Na-feldspar, and 12% mica, among other minerals.

which reveals that the main average particle size ranges from 0.14 to 0.24 mm and that the dominant contact type between the particles is linear. Generally, the whole rock is relatively dense, with a small number of primary intergranular pores.

We also performed a full-sample CT scanning of a representative rock sample using a CT setup<sup>33</sup> before conducting the fracturing experiment. As shown in Figure 2, the rock sample is composed of different particles, which are distinguished by different grayscale values.<sup>39</sup> These grayscale values are a function of the value of the attenuation coefficient ( $\mu$ ), which is typically referred to as the CT number (CTN). According to the definition of CTN<sup>39,40</sup> the scanned sandstone sample in this work (Figure 2b) is fairly dense and the degree of cementation is also strong. The scattered white particles and linear bands inside the rock indicate that it contains minerals with different properties, distributions, and particle sizes. We also observed the presence of natural bedding planes in this sample. From the images shown in Figures 1 and 2, we can conclude that the tight sandstone used in this work is a type of laminated sandstone and has initial bedding planes that are approximately in the transverse direction of the core.

**2.2. Experimental Equipment.** **2.2.1. SC-CO<sub>2</sub> Hydraulic Fracturing Setup.** We used a laboratory fracturing system that is designed for multiple fluids (such as CO<sub>2</sub> and water).<sup>33,41</sup> The setup consists of a pump, triaxial-loading system, sample holder, constant-temperature water bath system, control/measurement system, etc. (as shown in Figure 3). The pump is a plunger type and has a maximum pressure of 50 MPa. The triaxial-loading system is pressurized through

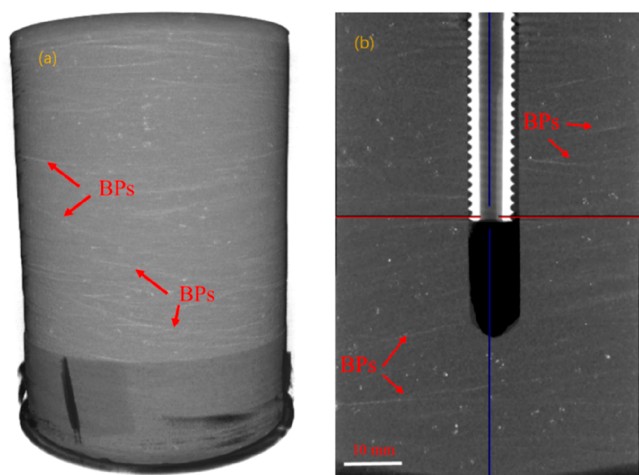


**Figure 2.** CT scanning image of sample before fracturing experiment: (a) external structure of full rock sample and (b) internal structure of middle-slice segmentation.

a hydraulic pump that can load the specimen up to 80 MPa in the longitudinal direction (axial stress,  $\sigma_a$ ) and in the circumferential direction (confining stress or pressure,  $P_c$ ). The measurement system can control the electric machine and vacuum pump and record pressure and temperature as they vary with time. The accuracy of the pressure measurement is  $\pm 0.1$  MPa (1%) and that of temperature is  $\pm 0.1$  °C (1%).

**2.2.2. CT Scanning Setup.** The “Zeiss Xradia 510 Versa” CT scanning system was used in this study and was discussed by Yang et al. (2020).<sup>33</sup> The resolution was 53  $\mu\text{m}$  at an X-ray working voltage of 120 kV and current of 62.5  $\mu\text{A}$  as used in this work. The CT scanning system works by emitting X-rays through rock samples and measuring their attenuation on the downstream end of the sample. The radiation intensity can be expressed by CTN, which reflects the details on the interior structure of the sample.<sup>42</sup> The entire rock sample can be scanned by this system before and after the fracturing experiment.

**2.3. Experimental Procedures.** Table 2 summarizes the different fracturing experiments that were performed with water and SC-CO<sub>2</sub> under different stress states. The sample was first heated to 40 °C in

an oven for 24 h before the experiment. The experimental sample was then placed in the triaxial core holder, and the target confining and axial stresses were applied to the sample. The vacuum pump was then triggered to test for blocking or leakage issues in all connecting pipelines. Next, CO<sub>2</sub> was injected into the booster pump until it was stabilized (normal pressure is 5.5–7.0 MPa). The constant-temperature water bath system was circulated to maintain the booster cylinder of the pump and sample holder at a specified temperature. Finally, the motor was triggered to inject fluid into the sample, and the pressure and temperature were recorded every 0.1 s until the rock broke and the pressure dropped sharply. After fracturing, we ran CT scans on the fractured samples in order to analyze the fracture morphology. Finally, we note that the experiments were repeated whenever we suspected an equipment error or the results did not appear consistent. This was to ensure that our fracture experiments and analyses are repeatable and representative of what happens in the subsurface.

### 3. RESULTS AND DISCUSSIONS

In this section, the results of our fracturing experiment with water and SC-CO<sub>2</sub> under various stress states are analyzed. We also discuss the formation breakdown pressure and reconstruction of the fracture patterns based on the CT images obtained. We then quantify the fracture properties using quantities (such as fractal dimension, area ratio, standard deviation of fracture aperture, etc.) that were estimated from the digital images. Furthermore, fracture attributes such as complexity, roughness, and fracture-induced capacity are characterized using this approach.

**3.1. Breakdown Pressure under Different Stress States.** **3.1.1. Theoretical Description.** As discussed in the introduction, fracture initiation and morphology may be influenced by several factors, such as the fracturing fluid, stress magnitudes, and rock heterogeneity, among others. Conventional fracture mechanics and continuum mechanics typically express fracture initiation as a function of the stress loading and tensile strength of the rock. Under a triaxial condition, the plane of fracture or parting first tends to be

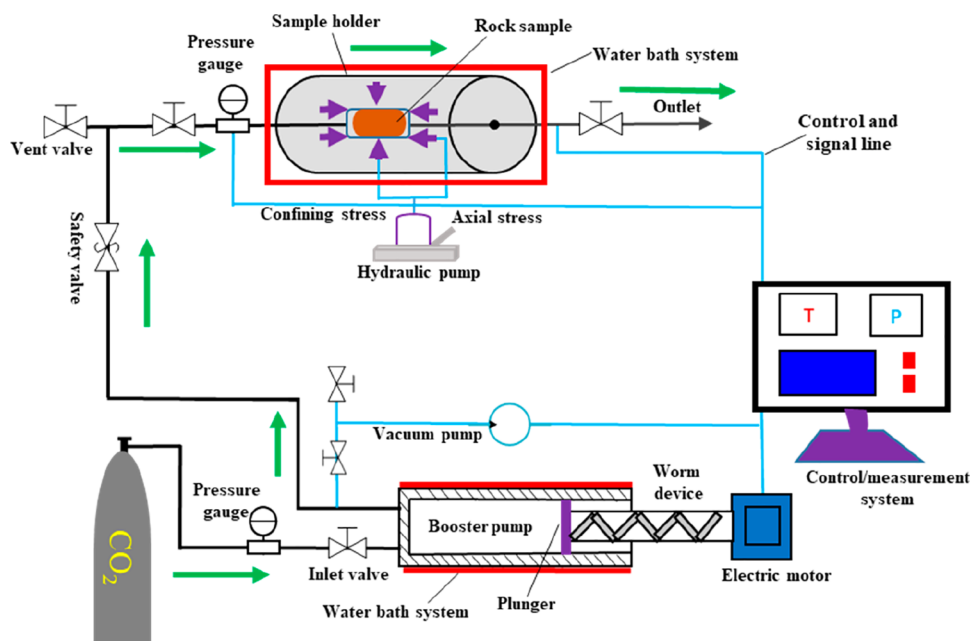


**Figure 3.** Schematic of the multiple fluid fracturing device.

Table 2. Experimental Schemes for the Fracturing Experiments<sup>a</sup>

number	fluid type	$T_f/^\circ\text{C}$	$T_r/^\circ\text{C}$	$Q_i$ (mL/min)	$\sigma_c \times \sigma_a/\text{MPa}$	CT scanning
A-0/1	water	25	25	10	10 × 15	A-0/1
A-2/3	SC-CO <sub>2</sub>	40	40	40	10 × 15	A-2/3
A-4/.../A-8	SC-CO <sub>2</sub>	40	40	40	5 × 5/10 × 10/15 × 15/20 × 20/25 × 25	A-7
A-9/.../A-13	SC-CO <sub>2</sub>	40	40	40	5 × 10/10 × 20/15 × 20/15 × 25/20 × 25	A-10
A-14/.../A-18	SC-CO <sub>2</sub>	40	40	40	10 × 5/15 × 10/20 × 10/20 × 15/25 × 20	A-16/A-17

<sup>a</sup> $T_p$ , fluid temperature;  $T_r$ , rock temperature;  $Q_i$ , fluid injection rate;  $\sigma_c$ , confining stress;  $\sigma_a$ , axial stress.

perpendicular to the least principal stress.<sup>26,43</sup> The formation breakdown pressure ( $P_b$ ) can be expressed as,<sup>44</sup>

$$P_b = 3\sigma_h - \sigma_H + \sigma_t - P_p \quad (1)$$

where  $\sigma_h$  and  $\sigma_H$  refer to the least and greatest horizontal stresses, respectively,  $\sigma_t$  is the tensile strength of rock, and  $P_p$  is the pore pressure. If the core sample is treated as an elastic medium with no pore spaces or pore pressure,  $P_b$  can be simplified as

$$P_b = 3\sigma_h - \sigma_H + \sigma_t \quad (2)$$

However, if there is natural pore pressure or fluid permeating into rock, the above equation (H–W) can be modified as,<sup>45,46</sup>

$$P_b = \frac{3\sigma_h - \sigma_H + \sigma_t - 2\eta P_p}{2(1 - \eta)} \quad (3)$$

where  $\eta = \alpha(1 - 2\nu)/(1 - \nu)$  is a function of  $\alpha$  and  $\nu$ . The symbol  $\alpha$  refers to the Biot constant, while  $\nu$  represents the Poisson ratio.

For the impermeable case ( $\alpha = 0$ ,  $P_p = 0$ ), this equation is expressed as

$$P_b = (3\sigma_h - \sigma_H + \sigma_t)/2 \quad (4)$$

Considering that our SC-CO<sub>2</sub> fracturing experiments were performed on cylindrical rock samples (as in Figure 4), we can

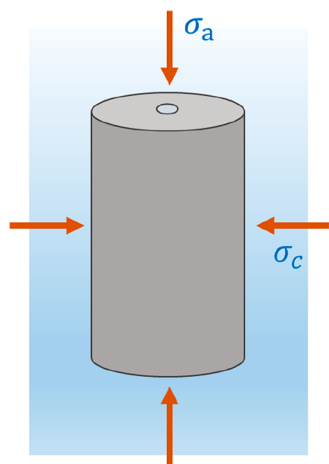


Figure 4. Schematic of stress loading on rock sample.

have three possible stress states. The first case is a triaxial compression test, where the least and intermediate horizontal stresses are equal and applied as the confining stress, which is less than the axial stress (that is,  $\sigma_{\min} = \sigma_h = \sigma_H = P_c < \sigma_a$ ). The second case is a triaxial extension test, where the confining stress is greater than the axial stress applied (that is,  $\sigma_a < P_c$ ). The third and final case is a hydrostatic test, where the confining and axial stresses are equal (that is,  $P_c = \sigma_a$ ).<sup>47</sup>

Considering the stress states discussed above, the revised expression for formation breakdown pressure can be given as,

$$P_b = \frac{A\sigma_a + B\sigma_c + C\sigma_t}{2 - \eta} \quad (5)$$

where  $\sigma_a$  and  $\sigma_c$  stand for the axial and confining stresses, respectively, and  $A$ ,  $B$ , and  $C$  refer to the coefficients of axial stress, confining stress, and tensile strength, respectively.

**3.1.2. Experiment Results of Fracturing with Water and SC-CO<sub>2</sub>.** **3.1.2.1. Breakdown Pressure of Rock Fractured by Water and SC-CO<sub>2</sub>.** The pump pressure was monitored and recorded against time during the injection of the fracturing fluid into rock. When the pressure reached the threshold strength of rock, the rock failed and the pressure declined sharply. Figure 5 gives the plot of the inlet pump pressure against time for both water and SC-CO<sub>2</sub> fracturing. It shows that the pressurization processes are different for water and SC-CO<sub>2</sub>, even though both processes are conducted at the same stress state. The pump pressure for water fracturing goes through two pressurization processes before it reaches the formation breakdown pressure. It increases slightly at the initial stage, then increases linearly for the remainder of the experiment, as shown. The results also show that the rock eventually fails (gets fractured) and the pressure drops abruptly. It is worth noting that the duration of the entire water fracturing process (40 s) is much shorter than that of the SC-CO<sub>2</sub> (Figure 5b) fracturing process, which lasts for 22 min. This could be attributed to the much lower compressibility of water in comparison to that of SC-CO<sub>2</sub>. Unlike the water fracturing process, the plot of the pump pressure for SC-CO<sub>2</sub> fracturing (Figure 5b) can be divided into three stages: the fluid pressure increases linearly and slowly for the first 12 min of the test, then the pressure increases rapidly until the formation breakdown pressure is reached, and finally the rock fails. After the rock fails in the third and final stage, the CO<sub>2</sub> leaks and expands from the borehole to the outlet of sample chamber.

The formation breakdown pressures of the rocks fractured by water and SC-CO<sub>2</sub> are shown in Table 3. It is notable that the rocks fractured by water have a higher breakdown pressure than those fractured by SC-CO<sub>2</sub>. The average magnitude of the formation breakdown pressure from SC-CO<sub>2</sub> fracturing was ~62% less than that from water fracturing, which means that SC-CO<sub>2</sub> can effectively decrease the formation breakdown pressure under the same stress conditions. This is because SC-CO<sub>2</sub> has a much lower viscosity and surface tension but a higher diffusivity than water. This makes it more likely to penetrate into the rock matrix and contribute to the buildup of local stresses in small pores, resulting in the reduction of effective normal stress. This consequently leads to a reduction in the formation breakdown pressure.<sup>27,48</sup> Similar results have been reported on fracturing experiments conducted on tight

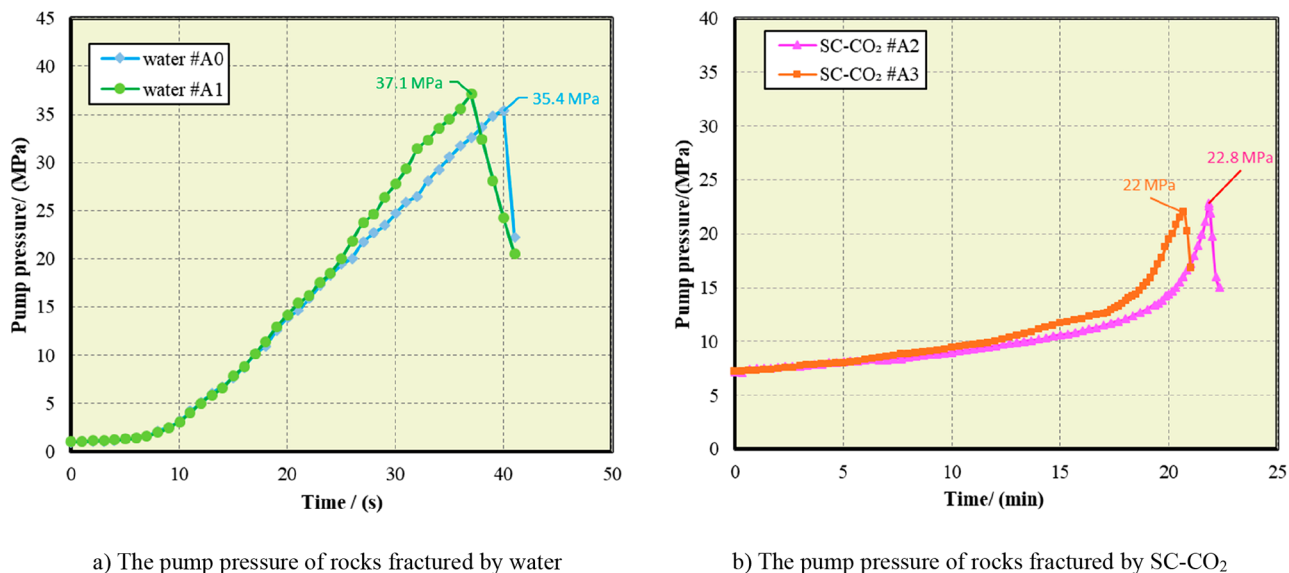


Figure 5. Plots of pump pressure versus time when fracturing with (a) water and (b) SC-CO<sub>2</sub>.

Table 3. Breakdown Pressure of Rocks Fractured by Water and SC-CO<sub>2</sub> at Different Stress States

group	fracturing fluid	$\sigma_c$ /MPa	$\sigma_a$ /MPa	breakdown pressure/MPa	
A-0/1	water	10	15	37.1	
				35.4	
A-2/3	SC-CO <sub>2</sub>	10	15	22	
				22.8	
case 1: $\sigma_c < \sigma_a$	SC-CO <sub>2</sub>	5	10	21.5	
			10	20	24.3
			15	20	28.1
			15	25	29.6
case 2: $\sigma_c > \sigma_a$	SC-CO <sub>2</sub>	10	5	16.5	
			15	10	23.4
			20	10	25.6
			20	15	27.2
case 3: $\sigma_c = \sigma_a$	SC-CO <sub>2</sub>	5	5	17.9	
			10	10	21.3
			15	15	27.5
			20	20	28.9
		25	25	37.6	

sandstone,<sup>32</sup> shale,<sup>25</sup> and granite<sup>49</sup> samples, as well as in numerical simulations.<sup>27,50</sup>

**3.1.2.2. Effect of Different Stress States on Formation Breakdown Pressure.** A series of sandstone specimens (listed in Table 2: A2–A18) were prepared for SC-CO<sub>2</sub> fracturing experiments under various stress conditions. To ensure the accuracy/reproducibility of the experiment, some of the tests were repeated when the experiment either failed or gave results with large deviations from the other experimental data. Table 3 outlines the formation breakdown pressures obtained when the fracturing experiment was conducted for the different samples under different stresses.

In case 1 (where the confining stress is less than the axial stress), the fracture tends to propagate along the borehole

(longitudinally) because fractures tend to open against the least principal stresses. This ensures that the energy needed to create a fracture is minimized. In this case, the least principal stress to be overcome by the injected fluid pressure is the confining stress, which acts horizontally. So, the fracture opens vertically against this minimum horizontal stress. As presented in Figure 6a, the value of breakdown pressure varies linearly with the confining pressure. In case 2 (where the confining stress is greater than the axial stress), the fracture may propagate horizontally across the borehole (transversely). This is because the least principal stress to be overcome by the injected fluid pressure is the axial stress, which acts vertically. Figure 6b shows that the formation breakdown pressure is a linear function of the axial stress. In case 3 (where the confining stress is equal to the axial stress), the breakdown pressure is a linear function of the confining or axial stress because they are equal in magnitude. The results are shown in Figure 6c. The fitting linear functions (from Figure 6) for each of these three cases are as follows: When the least principal stress is the confining stress ( $\sigma_{\min} = \sigma_c < \sigma_a$ ):

$$P_b = 0.9655\sigma_{\min} + 14.748 \quad (6)$$

When the least principal stress is the axial stress ( $\sigma_{\min} = \sigma_a < \sigma_c$ ):

$$P_b = 1.3792\sigma_{\min} + 9.7692 \quad (7)$$

When the least principal stress is the confining or axial stress ( $\sigma_{\min} = \sigma_a = \sigma_c$ ):

$$P_b = 0.94\sigma_{\min} + 12.56 \quad (8)$$

According to classical fracture mechanics, the reason for the change of breakdown pressure is that the injection pressure is used to overcome the least principal stress and some or all of the tensile strength of the rock, thereby causing rock failure. However, due to the applied stresses, the rock sample will rupture or open against the least principal stress. The linear relationship from the experimental results indicates that the pressure of the injected fluid needs to overcome both the rock tensile strength and the least principal stress.<sup>45</sup> The scatter in the plots in Figure 6 can be attributed to the heterogeneity in the material properties (such as rock tensile strength,

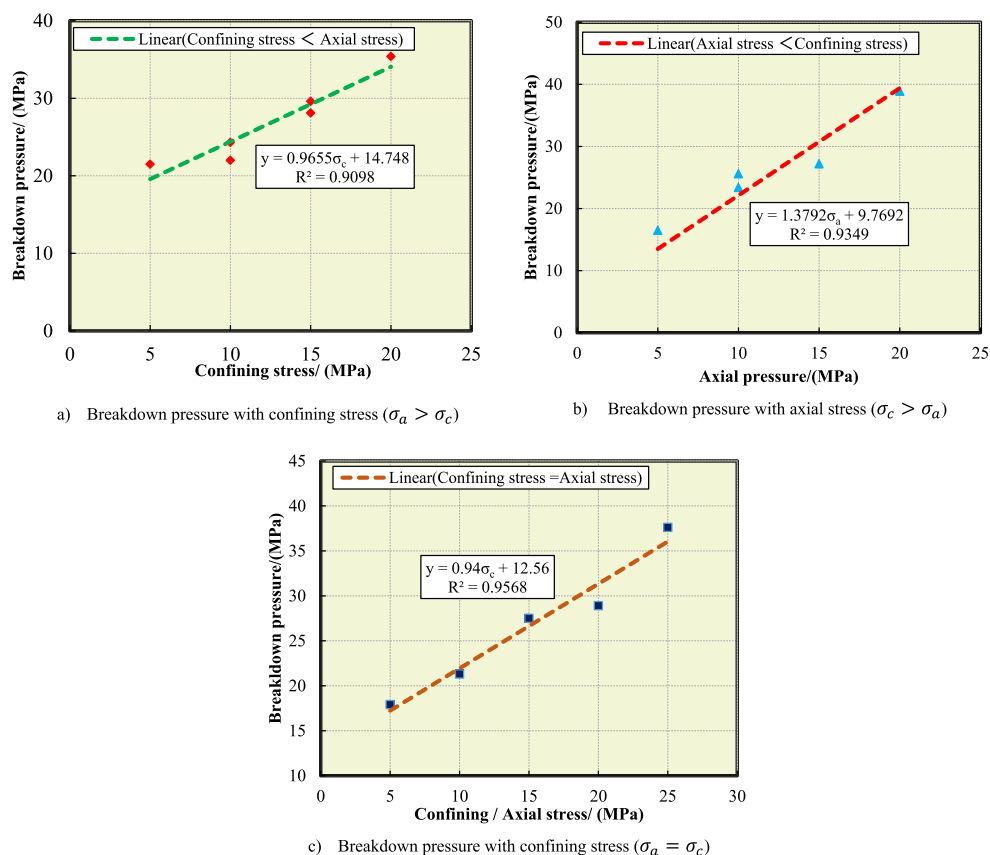


Figure 6. Breakdown pressure with confining/axial stress in various cases.

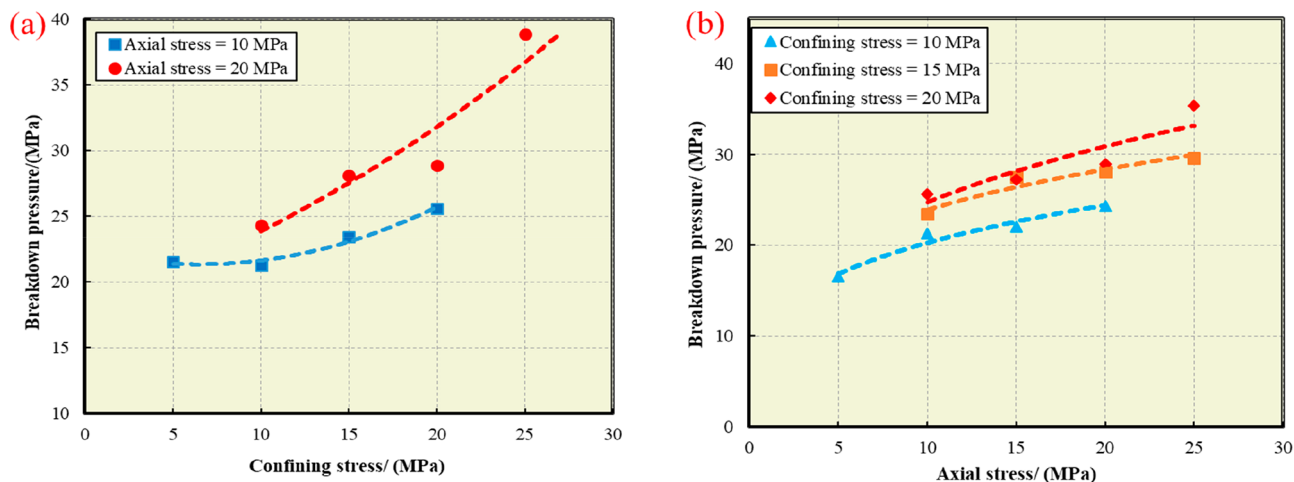


Figure 7. Breakdown pressure varied with confining and axial stress: (a) axial stress is fixed and (b) confining stress is fixed.

permeability, etc.), which could lead to stress concentrations in the rock and influence the formation breakdown pressure during the SC-CO<sub>2</sub> fracturing experiment.<sup>26</sup>

Additionally, from the experimental results in Figure 7, we observe that the formation breakdown pressure increases when one of the two stresses (say confining stress) is fixed and the other (say axial stress) is increased. When the axial stress is maintained at 10 and 20 MPa, the breakdown pressure increases (by 6% and 18%, respectively) as the confining stress increases (as shown in Figure 7a). Similarly, when the confining stress is fixed at 10, 15, and 20 MPa, the breakdown pressure approximately increases linearly as a function of the

axial stress and the average breakdown pressure increases by 14%, 8%, and 14%, respectively.

**3.2. Fracture Patterns and Morphologies Induced by Water and SC-CO<sub>2</sub>.** In this section, the fracture morphologies generated by water and SC-CO<sub>2</sub> fracturing are investigated using CT image reconstruction. We also characterized the effects of the differential stress ( $\sigma_1 - \sigma_3$ ) on the fracture patterns obtained from SC-CO<sub>2</sub> fracturing. Since the initial data collected from the CT scanning setup are a series of two-dimension (2D) slice images, we reconstructed the fracture using a post-processing software package that combines all these 2D images into a 3D rock model. However, it is difficult

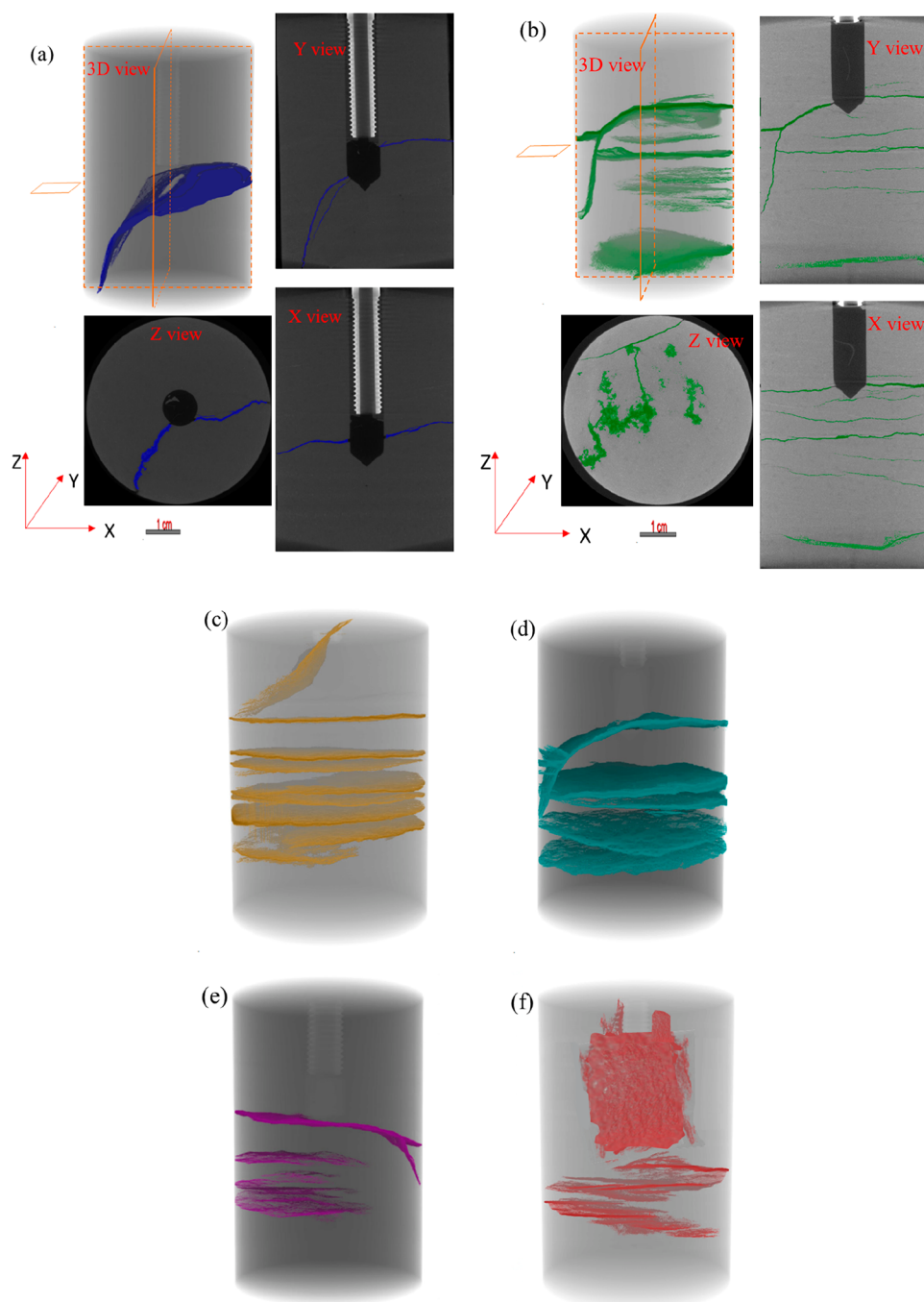


**Figure 8.** Full-sample reconstructed fracture morphologies under diversified differential stresses: (a) water fracturing at  $\sigma_c$  and  $\sigma_a$  of 10 and 15 MPa, respectively; (b) SC-CO<sub>2</sub> fracturing at  $\sigma_c$  and  $\sigma_a$  of 10 and 15 MPa, respectively; (c–f) SC-CO<sub>2</sub> fracturing under the  $\sigma_c$  and  $\sigma_a$  of  $20 \times 20$ ,  $20 \times 10$ , and  $10 \times 20$  MPa, respectively.

to view the fracture clearly from this 3D model since the fracture inside the rock is covered by the rock matrix. To view the fractures clearly, we applied a threshold method that allowed us to distinguish between the fracture and the rock matrix.<sup>51</sup> The CT scanner works by obtaining different count numbers (CTNs), which could be represented as grayscale values that vary from 0 to 255, indicating the variation in the components and properties of the rock. We typically differentiate between the fracture and matrix on the basis of these grayscale values. After the rock and fracture were reconstructed, we set all the fractures to a grayscale value of 1 and the matrix to a grayscale value 0, after which the fracture

can be easily segmented from the matrix.<sup>33</sup> Figure 8 shows the 3D reconstructed fracture morphologies obtained from water and SC-CO<sub>2</sub> fracturing under different stress states.

**3.2.1. Fracture Induced by Water and SC-CO<sub>2</sub>.** Figure 8a,b shows the reconstructed fracture generated by water and SC-CO<sub>2</sub> fracturing under identical stress states ( $\sigma_c$  and  $\sigma_a$  of 10 and 15 MPa, respectively). It can be seen from the different view directions that the rock fractured by water initiates from the bottom of borehole and then propagates transversely and longitudinally along two different directions. Besides this main fracture, one thin fracture branch along the longitudinal distribution is also induced near the main fracture. Although

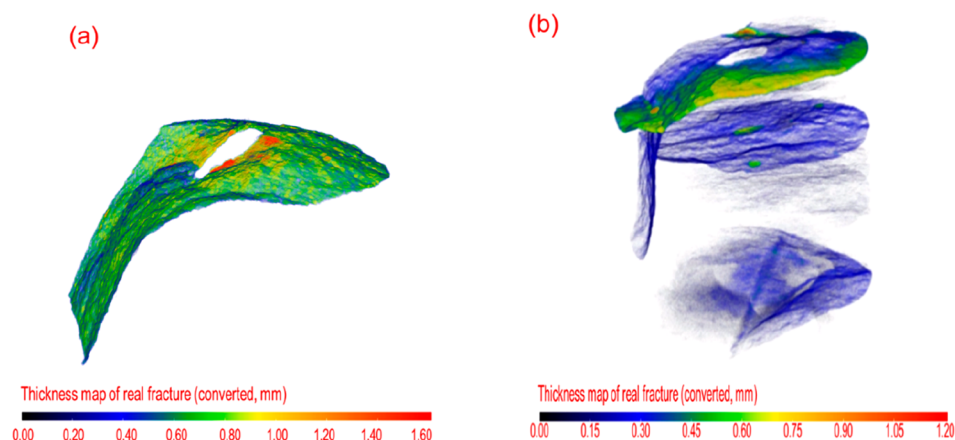


**Figure 9.** Thickness map of fractures induced by (a) water and (b) SC-CO<sub>2</sub>.

classical fracture mechanics theory indicates that the fractures should propagate along the longitudinal direction in this stress state (for homogeneous materials), the fracture actually propagates along the transverse direction because its propagation path is influenced by the presence of pre-existing bedding planes in an actual rock sample. Since rocks typically contain bedding planes, fractures are more likely to propagate along these planes of weakness in actual rocks. This indicates that the process of fracture propagation is controlled not only by the applied stresses but also by the heterogeneity in the material properties of the rock.

In comparison to the rock fractured by water (Figure 8a), the rock fractured by SC-CO<sub>2</sub> (Figure 8b) has a more complicated fracture geometry and morphology. The main fracture that initiated from the bottom of borehole has a similar propagation pattern to that induced by water. It first propagates through the transverse direction and nearly horizontal bedding plane. However, unlike with the rock fractured by water, we observed seven fracture branches or secondary fractures (besides the main fracture), most of which distribute in the subhorizontal direction. This result indicates that rocks fractured by SC-CO<sub>2</sub> can induce more fracture branches and more complicated fracture networks in comparison to those fractured by water. Furthermore, the rock heterogeneity shows a greater effect on the fracture propagation than the stress state in this work. The reason that SC-CO<sub>2</sub> induced more complicated fracture patterns can be attributed to its special properties, such as zero surface tension and strong mobility, which makes it easy to percolate into smaller pore spaces and contributes to the buildup of local stress concentrations. SC-CO<sub>2</sub> can realize local pressurization as the duration of the experiment is longer, resulting in more secondary and branching fractures. This can be confirmed by the fact that some of the secondary fractures are not directly connected with the main fracture.

**3.2.2. Effect of Differential Stress on the Fracture Patterns.** In order to investigate the effect of the applied differential stress on fracture propagation induced by SC-CO<sub>2</sub>, the representative rock samples were scanned to analyze the fracture morphology. Figure 8c–f shows the reconstructed 3D fracture morphology under differential stresses of 0, 5, and 10 MPa. When the confining stress is equal to the axial stress (Figure 8c), a main fracture initiates from the bottom of the borehole and propagates obliquely to the rock boundary. At the same time, nearly 10 secondary and branching fractures are

generated, most of which have a similar propagation direction, which is along the horizontal direction in general. This indicates that, when the stress difference is 0, fracture networks with several branches are formed and the propagation directions are roughly identical. When the stress difference is 5 MPa (Figure 8b,d), the main fracture propagation direction conforms to the classical fracture mechanics, which indicates that fractures should propagate along the direction of the maximum principal stress. Besides, there are five branching fractures (Figure 8d) induced as well, and the direction of propagation is nearly transverse. When the stress difference is 10 MPa (Figure 8e,f), the fractures generated under two different stresses show that the main fractures propagate approximately along the direction of the maximum principal stress, while the branching fractures are similarly affected by rock heterogeneity and propagate in the transverse direction. The reconstructed fracture morphologies under various stress states suggest that small differential stresses tend to induce fracture networks with more branches, whereas large differential stresses create relatively simple fracture patterns. More importantly, the initial bedding planes and pre-existence of thin fractures have a significant impact on the fracture propagation. These experimental results with respect to the effect of stress state on laminated tight sandstone are in agreement with the previous investigation results reported by Zhang et al. (2017) and He et al. (2020).<sup>34,35</sup>

**3.3. Fracture Quantification Based on Reconstruction of CT Images.** Fracture complexity and roughness are two significant characteristics used to describe fracture morphology.<sup>52</sup> In this section, we quantitatively analyze the fracture characteristics based on CT image digitization and a related algorithm. The fractal dimension, fracture volume, and standard deviation of aperture and fracture area ratio are used to investigate the fracture attributes of the entire rock sample. After the fracture phase is extracted from reconstructed rock through the threshold approach, fracture digitization and other post-processing were further performed to obtain quantitative results.<sup>33</sup>

### 3.3.1. Quantification Description and Algorithm.

**3.3.1.1. Fractal Dimension.** As a geometry analysis parameter, the fractal dimension (FD) is a ratio that provides a statistical index of complexity, which can be employed to evaluate the complexity of a fracture.<sup>53</sup> The box-counting method was used to calculate the fractal dimension in this work because it is not limited by any dimension or patterns with or without self-

similarity.<sup>54</sup> This method was realized by filling boxes (cubic) with different sizes ( $h$ ) into a geometry and then acquiring the relation between the box number,  $N_h$ , and size  $h$ . The FD is defined mathematically as

$$FD = \lim_{h \rightarrow 0} \frac{\ln(N_h)}{\ln\left(\frac{1}{h}\right)} \quad (9)$$

Due to the fact that the image is represented by voxels, a fracture can be digitized by setting the voxel size  $s$  (unit size of each voxel, which is resolution,  $r$ , in this work).<sup>55</sup> Additionally, the variables  $N_h$  and  $h$  can be obtained by filling boxes with different sizes into the digitized fracture and plotting  $N_h$  against  $h$  in a log–log plot. The FD was obtained as the slope of the straight line in this log–log plot.<sup>56–58</sup>

**3.3.1.2. Fracture Aperture and Standard Deviation.** Fracture aperture,  $t$ , is a significant parameter that is used to describe the fracturing characteristic. In previous publications, the aperture was also determined by different methods, such as an optical measurement from an ordinary rock picture<sup>38</sup> and obtaining the fracture aperture from local 3D X-ray scans of the fracture surface.<sup>31,32</sup> However, these two methods are either not accurate or cannot collect data for an entire fracture. In this study, the aperture of the whole fracture can be obtained on the basis of fracture digitization. The fracture is digitized by several voxels of size  $r$ , which means that the fracture is represented by small cubic boxes. So, the aperture of fracture can be calculated by

$$t = r \times n \quad (10)$$

where  $r$  is the resolution of the setup (which is 53  $\mu\text{m}$  in this work), while  $n$  refers to the number of voxels in the direction of the normal to a fracture surface (making up the fracture aperture). As shown in Figure 9, the aperture map calculated from a commercial software package depicts the fracture thickness at different locations on the fracture surface. We also obtained basic descriptive statistical data on the fracture aperture (such as minimum, maximum, and mean of the fracture aperture). Considering that the fracture aperture is composed of a large amount of data at different locations, the standard deviation (SD) of the aperture was calculated to quantify the degree of deviation of the fracture aperture from its average value. This standard deviation can be used to indicate the roughness of the fracture surface and is given as

$$SD = \sqrt{\frac{1}{N-1} \sum_{i=1}^N (t_i - \bar{t})^2} \quad (11)$$

where  $N$  refers to the statistical number of fracture aperture,  $t_i$  is the fracture aperture of each statistical point, and  $\bar{t}$  is the average value of the fracture aperture.<sup>36</sup>

**3.3.1.3. Fracture Volume and Volume Fraction.** Fracture volume is a significant parameter for evaluating fracturing performance. As the extracted fractures are digitized by a series of voxels, the fracture volume can be calculated by taking the sum of the volume all the voxels that comprise the full fracture. The total fracture volume  $V_t$  is obtained as

$$V_t = V_0 \times N_t \quad (12)$$

where  $N_t$  is the total number of voxels and  $V_0$  is the volume of each voxel, which is given as  $V_0 = r^3$ . The fracture volume fraction ( $\alpha$ ) was determined to evaluate the fracture-induced capacity for different fluids or under different stress states. It is

a ratio of the volume of the fracture network ( $V_t$ ) to the effective volume of the scanned rock sample:

$$\alpha = V_t/V_s \quad (13)$$

where  $V_s$  is the effective volume of scanned rock sample ( $V_s = V - V_b$ ),  $V$  refers to the total volume of the scanned sample, and  $V_b$  refers to the borehole volume contained in the scanned sample.

**3.3.1.4. Fracture Area Ratio.** The fracture area ratio (AR) is defined as the ratio of the actual fracture area ( $s_f$ ) to the projected area ( $s_p$ ). The common approach for obtaining the fracture area  $s_f$  is by calculating the ratio of the total fracture volume to the average fracture thickness, but this may result in some errors. In order to estimate the fracture area more accurately, a fracture skeleton (or fracture medial surface) is introduced to represent the fracture area. The medial skeleton of a shape is a thin version of that shape, which is typically used to emphasize geometrical and topological properties of the shape, such as its connectivity, topology, length, direction, and width.<sup>59</sup> In this work, the most popular method, named homotopic thinning,<sup>60–63</sup> was used to obtain the fracture skeleton. The projected area ( $s_p$ ) is the cross-sectional area of the rock minus the area of the borehole, if the fracture passes through the borehole. Both AR and SD of fracture aperture were used to characterize fracture complexity,<sup>26,36,48</sup>

$$AR = \frac{s_f}{s_p} \quad (14)$$

where  $s_f$  is the fracture area, which can be obtained by taking the sum of the area of each pixel in the medial skeleton.

**3.3.2. Quantification of Fractures Based on CT Image Digitization.** The fractal dimension of a fracture (computed using eq 9) is based on fracture digitization. As shown in Figure 10, the FD induced by SC-CO<sub>2</sub> (average of 2.22) is

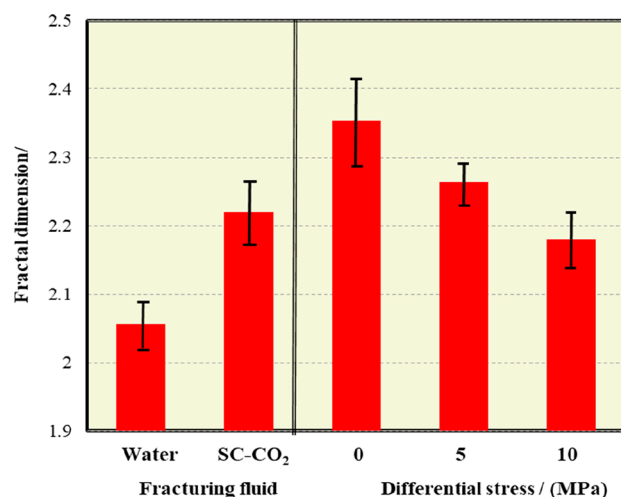


**Figure 10.** FD values of fractures induced by water and SC-CO<sub>2</sub> under various differential stresses.

larger than that generated by water (average of 2.056) under the same stress state. It indicates that SC-CO<sub>2</sub> can create more complex fractures than water at the conditions of this experiment. Various researchers, such as Jia et al. (2018)<sup>31</sup> and Li et al. (2019),<sup>32</sup> have also presented similar results. Furthermore, the FD of fractures induced by SC-CO<sub>2</sub> fracturing under various differential stresses could be obtained

using the same approach. Figure 10 shows that the FD tends to drop slightly with increasing differential stress, the averages of which are 2.354, 2.263, and 2.18 for differential stresses of 0, 5, and 10, respectively (the specific results are listed in appendix Table 4). This result indicates that small differential stresses may contribute to the creation of relatively complex fractures, while higher differential stresses tend to facilitate the creation of simple fractures. This quantitative result is also consistent with the fracture geometry and pattern described in section 3.2.

Additionally, the AR obtained from the fracture skeleton and eq 14 was also used to evaluate the fracture complexity. Figure 11 indicates that SC-CO<sub>2</sub> can create twice larger fracture areas

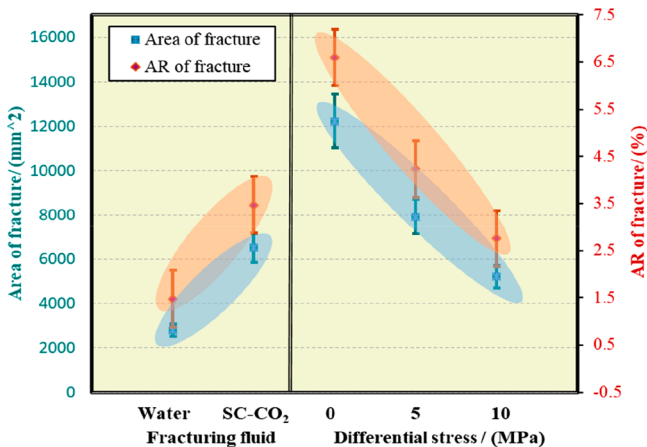


**Figure 11.** Area of fracture surface and the ratio induced by water and SC-CO<sub>2</sub>.

and AR than those induced by water (AR values of 1.47 and 3.47 for fractures induced by water and SC-CO<sub>2</sub>, respectively). This is consistent with results published by Wang et al. (2016),<sup>48</sup> Zhao et al. (2018),<sup>36</sup> Li et al. (2019),<sup>32</sup> etc. The AR values of fractures generated under stress differences demonstrate that a larger stress difference can create a smaller AR value; the average AR values of fractures induced under stress differences of 0, 5, and 10 are 6.60, 4.24, and 2.76, respectively. This result indicates that fractures induced by SC-CO<sub>2</sub> have a higher complexity in comparison to those induced by water fracturing under the same condition. Furthermore, larger differential stresses may induce simple fractures, whereas smaller differential stresses tend to induce fractures with a higher complexity. This is also consistent with the quantitative analysis of fractal dimensions.

The fracture aperture was obtained on the basis of fracture digitization and eq 10. The results shown in Figure 12 indicate that the average aperture induced by water (0.409) is thicker than that created by SC-CO<sub>2</sub> (0.319) but that the SD of the fracture aperture induced by water (0.124) is smaller than that induced by SC-CO<sub>2</sub> (0.207). This suggests that, although water can create thicker fractures, most of the apertures concentrate around the average value, resulting in a relatively smaller SD in the fracture aperture. Furthermore, the roughness of the fracture surface induced by water is smaller, so the fracture is smoother and more uniform. On the contrary, SC-CO<sub>2</sub> fracturing can create fractures with lower average fracture apertures but greater SD of fracture aperture (than that induced by water). This means that, even though the fractures induced by SC-CO<sub>2</sub> fracturing are relatively narrower

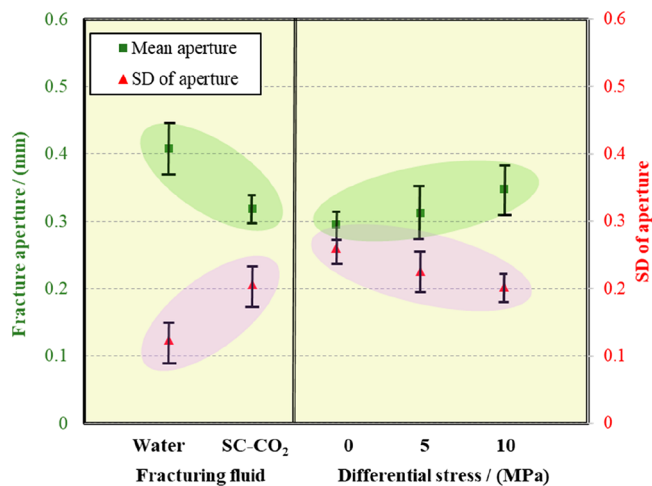


**Figure 12.** Mean aperture and SD of aperture created by water and SC-CO<sub>2</sub>.

than those induced by water fracturing, the distribution of the fracture aperture is more dispersed, resulting in higher values of surface roughness.

When the rock samples are fractured by SC-CO<sub>2</sub> under different stress states, the fracture aperture and SD were calculated. The results (Figure 12) demonstrate that the fracture aperture increases as the stress difference increases from 0 to 10 MPa, with mean apertures of 0.295, 0.3125, and 0.348 mm, respectively (more details are given in appendix Table 5). The SD of the fracture aperture induced under these differential stresses shows an opposite tendency with respect to aperture. That is, the larger stress difference can facilitate the creation of fracture surfaces with less roughness. On the contrary, smaller stress differences can induce narrower fractures with more surface roughness.

The fracture volumes induced by water and SC-CO<sub>2</sub> under different magnitudes of differential stresses are also quantitatively characterized on the basis of fracture digitization and eq 12. The volume fraction is also calculated to evaluate the fracture-induced capacity. As shown in Figure 13, fractures generated by SC-CO<sub>2</sub> have 4 times larger volume and volume fraction than those induced by water fracturing under the same stress condition (the volumes are 4053.37 and 948.15 mm<sup>3</sup>, while the volume the fractions are 3.04 and 0.705 for SC-CO<sub>2</sub>

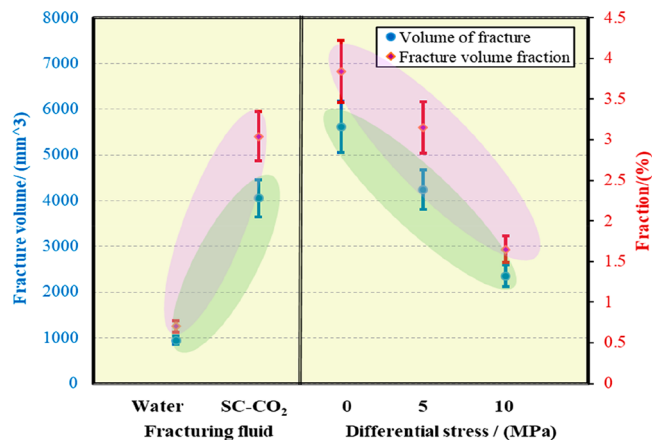


**Figure 13.** Fracture volume and the fraction induced by water and SC-CO<sub>2</sub>.

and water, respectively; additional parameters are listed in appendix Table 6). This illustrates that, although the mean apertures of fractures induced by SC-CO<sub>2</sub> fracturing are narrower, they tend to induce more fracture branches, so the fracture volume will be more than that created by water fracturing. It also indicates that SC-CO<sub>2</sub> has a higher fracture-induced capacity than water under this experimental condition. Moreover, the fracture volume and volume fraction induced by SC-CO<sub>2</sub> under the various stress differences are also computed. As shown in Figure 13, it is notable that the fracture volume and volume fraction both decrease with increasing differential stress. The volumes are 5615.04, 4240.8, and 2356.07 mm<sup>3</sup>, while the volume fractions are 3.84, 3.15, and 1.65 at differential stresses of 0, 5, and 10 MPa, respectively. This indicates that high stress differences may contribute to the creation of thicker but fewer fractures, and the fracture-induced capacity is relatively worse than that induced under low stress differences.

The creation of fracture networks that optimize oil and gas production requires a massive number of fractures, as well as the propagation of fractures further along the direction of maximum principal stress. Considering that fracture propagation is significantly impacted by the presence of bedding planes and pre-existing fractures, fractures may propagate transversely under different conditions, which is not always toward the direction of maximum principal stress. Our experimental results indicate that the fracture volume appears to be a reliable indicator for fracturing capacity because all the rock samples used in this work were cored from the same outcrop and have similar heterogeneity.

According to the above quantification characteristics of full-sample fractures, the fractures induced by SC-CO<sub>2</sub> fracturing are relatively narrower and have a larger volume fraction, complexity, and roughness than those created by water under the same stress condition. This may be attributed to the difference in the fluid properties of these two fracturing fluids. Given that SC-CO<sub>2</sub> has a lower viscosity and zero surface tension, it can easily penetrate to the rock matrix and smaller pore throats and cause a localized increase in pore pressure. This could lead to the creation of more fracture branches of different sizes and more surface roughness and complexity. The higher viscosity of water could create a larger fluid lag at the fracture tip, which could create relatively smooth fracture surfaces.<sup>31</sup> Moreover, the low compressibility of water could limit the supply of continuous pressure after rock breakdown without injection, leading to the creation of relatively simple fracture patterns. When fractures are initiated by highly compressible SC-CO<sub>2</sub>, the energy stored in the SC-CO<sub>2</sub> is released to further extend the initial fractures during phase change, resulting in high-speed fracture propagation, which consequently leads to the creation of more complex fracture patterns and branches.<sup>64</sup>

The results of SC-CO<sub>2</sub> fracturing in tight sandstones under various differential stresses show that large differential stresses tend to produce fracture networks with larger apertures but smaller fracture volumes and fracture complexity and lower roughness. At small differential stresses, the induced fracture has more branches, larger fracture volume, and higher complexity and roughness. This could be attributed to the fact that high differential stresses tend to release the energy of the injected fluid along a certain direction, thus forming a small number of fractures with large apertures. On the contrary, at low differential stresses, the energy of the injected fluid will be

released in all directions, resulting in the generation of new fractures that propagate in different directions. Although fractures are relatively narrow in aperture, the presence of several fracture branches tends to facilitate the development of conductive fracture networks. In field applications, proppants are pumped to keep the fractures open and further enhance oil and gas production.<sup>2,3</sup>

#### 4. CONCLUSIONS

In this work, we conducted fracturing experiments on tight sandstones using water and SC-CO<sub>2</sub> and under different stress states. The breakdown pressures of rocks fractured by water and SC-CO<sub>2</sub> were investigated, and a novel fracture reconstruction and quantification method was proposed on the basis of full-sample rock CT images. Using this approach, we performed a quantitative analysis of the fracture characteristics and effects of differential stress on fracture propagation.

Our experimental results indicate that SC-CO<sub>2</sub> fracturing can effectively reduce the formation breakdown pressure by approximately 60% in comparison to water fracturing. The SC-CO<sub>2</sub> fracturing experiments under different stress states indicate that the formation breakdown pressure varies linearly with the least principal stress. When the axial (or confining) stress is kept constant, the formation breakdown pressure shows a positive correlation with the confining (or axial) stress.

Our analysis of fracture morphology based on CT image reconstruction indicates that SC-CO<sub>2</sub> fracturing creates more complex fracture networks than water fracturing. We also observe that the complexity of the fracture geometry and pattern induced by SC-CO<sub>2</sub> fracturing increases as the magnitude of differential stress decreases. In general, the main fractures tend to propagate in the direction of the greatest principal stress. However, fracture propagation is also affected by the presence of bedding planes and pre-existing fractures. The new or secondary fractures tend to preferentially propagate along these bedding planes and fractures.

The results of our quantification of fracture morphology suggest that SC-CO<sub>2</sub> fracturing yields two times more fracture complexity and more (67%) surface roughness than water fracturing under identical stress conditions. Although the fractures induced by SC-CO<sub>2</sub> are relatively narrower than those induced by water, the volume fractions ( $\alpha$ ) of the SC-CO<sub>2</sub> fractures are 4 times greater than those created by water fracturing. This indicates that the SC-CO<sub>2</sub> fractures have better fracture-induced capacity under the same stress state. Our experimental results also indicate that the complexity, roughness, and volume fraction of fractures gradually reduce as differential stress increases. This implies that small stress deviations tend to create complex fracture networks, while a large differential stress is more likely to create a simple fracture with fewer fracture branches.

The fracture quantification approach we propose (based on CT images) can facilitate a nondestructive analysis of fractures induced in an entire rock sample. The fracture morphology obtained from CT reconstruction can be applied in fracture models for simulating real fracture networks. However, the method is limited by the size of the rock sample and experimental setup. At present, we can only scan rock samples less than 100 mm in size. Furthermore, the resolution of the scanning setup decreases with an increase in the size of the rock sample, which in turn limits the characterization of very small fractures. Therefore, to improve the accuracy of our experimental results in a future study, an improvement in the

scanning resolution and control of rock sample size will be required.

## ■ APPENDIX TABLES

**Table A4. FD Induced by Water and SC-CO<sub>2</sub> under Different Stress States**

sample	fracturing fluid	$\sigma_c \times \sigma_a$ /MPa	FD
A-0/1	water	10 × 15	2.064
			2.048
A-2/3	SC-CO <sub>2</sub>	10 × 15	2.1914
			2.253
A-10	SC-CO <sub>2</sub>	10 × 20	2.184
A-16	SC-CO <sub>2</sub>	20 × 10	2.176
A-17	SC-CO <sub>2</sub>	20 × 15	2.274
A-7	SC-CO <sub>2</sub>	20 × 20	2.354

**Table A5. Aperture Induced by Water and SC-CO<sub>2</sub> under Different Stress States**

fracturing fluid	$\sigma_c \times \sigma_a$ /MPa	$t_{max}$ /mm	$t_{min}$ /mm	$t_{mean}$ /mm	SD
water	10 × 15	1.461	0.124	0.431	0.108
		1.21	0.159	0.386	0.14
SC-CO <sub>2</sub>	10 × 15	1.18	0.102	0.323	0.2
		1.10	0.078	0.315	0.214
SC-CO <sub>2</sub>	10 × 20	1.23	0.0745	0.344	0.207
		1.14	0.082	0.352	0.198
	20 × 15	1.054	0.14	0.31	0.238
		1.13	0.086	0.295	0.261

**Table A6. Fracture Volume and Fraction**

fracturing fluid	$\sigma_c \times \sigma_a$ /MPa	$V_f$ /mm <sup>3</sup>	scanning size ( $\phi$ /H)/mm	borehole size ( $\phi$ /h)/mm	$V_s$ /mm <sup>3</sup>	fraction/%
water	10 × 15	852.56	49.86/66.1	9.58/31.45	127 247.98	0.67
		1043.75	49.76/73.28	9.25/21.84	142 506.96	0.74
SC-CO <sub>2</sub>	10 × 15	4250.03	49.62/68.58	9.63/11.69	132 617.51	3.23
		3856.71	49.80/70.47	9.84/24.6	135 323.41	2.85
SC-CO <sub>2</sub>	10 × 20	2440.13	49.82/68.5	9.73/11.43	132 615.62	1.84
		2274	50.15/79.8	9.81/23.47	155 775.51	1.46
	20 × 15	4231.56	49.74/63.7	9.62/14.6	122 653.86	3.453
		5165.04	49.52/70.3	9.58/11.4	134 506.25	3.84

## ■ AUTHOR INFORMATION

### Corresponding Author

**Haizhu Wang** – State Key Laboratory of Petroleum Resources and Prospecting, China University of Petroleum, Beijing 102249, China; [orcid.org/0000-0002-9164-2759](https://orcid.org/0000-0002-9164-2759); Phone: +86 010 89732176; Email: [whz0001@126.com](mailto:whz0001@126.com)

### Authors

**Bing Yang** – State Key Laboratory of Petroleum Resources and Prospecting, China University of Petroleum, Beijing 102249, China

**Zhonghou Shen** – State Key Laboratory of Petroleum Resources and Prospecting, China University of Petroleum, Beijing 102249, China

**Olufemi Olorode** – Craft & Hawkins Department of Petroleum Engineering, Louisiana State University, Baton Rouge, Louisiana 70803, United States; [orcid.org/0000-0002-7783-1406](https://orcid.org/0000-0002-7783-1406)

**Bin Wang** – Craft & Hawkins Department of Petroleum Engineering, Louisiana State University, Baton Rouge, Louisiana 70803, United States

**Yong Zheng** – State Key Laboratory of Petroleum Resources and Prospecting, China University of Petroleum, Beijing 102249, China

**Wanjuan Yan** – State Key Laboratory of Petroleum Resources and Prospecting, China University of Petroleum, Beijing 102249, China

**Zhaoyang Jia** – State Key Laboratory of Petroleum Resources and Prospecting, China University of Petroleum, Beijing 102249, China

Complete contact information is available at: <https://pubs.acs.org/10.1021/acs.energyfuels.0c03554>

### Notes

The authors declare no competing financial interest.

## ■ ACKNOWLEDGMENTS

This study was funded by the Natural Science Foundation of China (Grant Nos. 51922107, 51874318, and 41961144026) and the Strategic Cooperation Technology Projects of CNPC and CUPB (Grant No. ZLZX2020-01). The part of image data used in this study is available at <https://www.digitalrockportal.org/projects/285>.

## ■ REFERENCES

- (1) Wang, B.; Li, G.; Huang, Z.; et al. Hydraulics Calculations and Field Application of Radial Jet Drilling. *SPE Drilling & Completion* **2016**, *31* (1), 1.
- (2) Zhou, Y.; Ni, H.; Shen, Z.; et al. Study on Proppant Transport in Fractures of Supercritical Carbon Dioxide Fracturing[J]. *Energy Fuels* **2020**, *34*, 6186–6196.
- (3) Zheng, Y.; Wang, H.; Yang, B.; Hu, Y.; Shen, Z.; Wen, H.; Yan, W. CFD-DEM simulation of proppant transport by supercritical CO<sub>2</sub> in a vertical planar fracture. *J. Nat. Gas Sci. Eng.* **2020**, *84*, 103647.
- (4) Chen, J.; Zhou, L.; Li, H.; et al. Comparison on hydraulic and mechanical responses to the growing loading between both fractures induced by hydraulic fracturing and Brazilian splitting. *Energy Fuels* **2020**, *34*, 10933–10946.
- (5) Osborn, S. G.; Vengosh, A.; Warner, N. R.; Jackson, R. B. Methane contamination of drinking water accompanying gas-well drilling and hydraulic fracturing. *Proc. Natl. Acad. Sci. Unit. Proc. Natl. Acad. Sci. U. S. A.* **2011**, *108*, 8172–8176.
- (6) Vengosh, A.; Jackson, R. B.; Warner, N.; Darrach, T. H.; Kondash, A. A critical review of the risks to water resources from unconventional shale gas development and hydraulic fracturing in the United States. *Environ. Sci. Technol.* **2014**, *48*, 8334–8348.
- (7) Bahrami, H.; Rezaee, R.; Clennell, B. Water blocking damage in hydraulically fractured tight sand gas reservoirs: An example from

Perth Basin, Western Australia. *J. Pet. Sci. Eng.* **2012**, *88–89*, 100–106.

(8) Fenghour, A.; Wakeham, W. A.; Vesovic, V. The viscosity of carbon dioxide. *J. Phys. Chem. Ref. Data* **1998**, *27*, 31–44.

(9) Gupta, A. P.; Gupta, A.; Langlinais, J. Feasibility of Supercritical Carbon Dioxide as a Drilling Fluid for Deep Underbalanced Drilling Operation. SPE Annual Technical Conference and Exhibition, Dallas, TX, October 9–12, 2005.

(10) Du, Y.; Wang, R.; Ni, H.; et al. Application prospects of supercritical carbon dioxide in unconventional oil and gas reservoirs [J]. *Adv. Mater. Res.* **2012**, *S24*, 1355–1358.

(11) Wang, H.; Li, G.; Shen, Z. A Feasibility analysis on shale gas exploitation with supercritical carbon dioxide. Energy Sources Part A Recover. *Energy Sources, Part A* **2012**, *34*, 1426–1435.

(12) Wang, H.; Li, G.; Shen, Z.; et al. Expulsive force in the development of CO<sub>2</sub> sequestration: application of SC-CO<sub>2</sub> jet in oil and gas extraction[J]. *Front. Energy* **2019**, *13* (1), 1–8.

(13) Middleton, R. S.; Carey, J. W.; Currier, R. P.; et al. Shale gas and non-aqueous fracturing fluids: Opportunities and challenges for supercritical CO<sub>2</sub>. *Appl. Energy* **2015**, *147*, 500–509.

(14) Odumabo, S. M.; Karpyn, Z. T.; Ayala, H. L. F. Investigation of gas flow hindrance due to fracturing fluid leakoff in low permeability sandstones. *J. Nat. Gas Sci. Eng.* **2014**, *17*, 1–12.

(15) Kollé, J. Coiled-Tubing Drilling with Supercritical Carbon Dioxide, SPE/CIM International Conference on Horizontal Well Technology, Calgary, Alberta, Canada, November 6–8, 2000.

(16) Li, G.; Shen, Z.; Huang, Z. Research and applications of novel jet techniques in well drilling, completion and fracturing. *Sci. Found. China* **2014**, *2*, 43.

(17) Li, G.; Wang, H.; Shen, Z. et al. Supercritical carbon dioxide jet fracturing using coiled-tubing. China Patent CN102168545A, 2011; pp 8–31.

(18) Alemu, B. L.; Aagaard, P.; Munz, I. A.; Skurtveit, E. Caprock interaction with CO<sub>2</sub>: A laboratory study of reactivity of shale with supercritical CO<sub>2</sub> and brine. *Appl. Geochem.* **2011**, *26*, 1975–1989.

(19) Wang, H.; Li, G.; Shen, Z.; et al. Experiment on rock breaking with supercritical carbon dioxide jet. *J. Pet. Sci. Eng.* **2015**, *127*, 305–310.

(20) Zhang, L.; Wang, Y.; Miao, X.; Gan, M.; Li, X. Geochemistry in geologic CO<sub>2</sub> utilization and storage: A brief review. *Adv. Geo-Energy Res.* **2019**, *3* (3), 304–313.

(21) Zhou, J.; Hu, N.; Xian, X.; Zhou, L.; Tang, J.; Kang, Y.; Wang, H. Supercritical CO<sub>2</sub> fracking for enhanced shale gas recovery and CO<sub>2</sub> sequestration: Results, status and future challenges. *Adv. Geo-Energy Res.* **2019**, *3* (2), 207–224.

(22) Ishida, T.; Chen, Q.; Mizuta, Y.; Roegiers, J.-C. Influence of fluid viscosity on the hydraulic fracturing mechanism. *J. Energy Resour. Technol.* **2004**, *126* (3), 190–200.

(23) Ishida, T.; Aoyagi, K.; Niwa, T.; Chen, Y.; Murata, S.; Chen, Q.; Nakayama, Y. Acoustic emission monitoring of hydraulic fracturing laboratory experiment with supercritical and liquid CO<sub>2</sub>. *Geophys. Res. Lett.* **2012**, *39*, L16309.

(24) Inui, S.; Ishida, T. et al. AE monitoring of Hydraulic Fracturing Experiments in Granite Blocks Using supercritical CO<sub>2</sub>, Water and Viscous Oil. *48th U.S. Rock Mechanics/Geomechanics Symposium*, Minneapolis, MN, June 1–4, 2014; American Rock Mechanics Association: Alexandria, VA, 2014.

(25) Bennour, Z.; Ishida, T.; Nagaya, Y.; Chen, Y.; Nara, Y.; Chen, Q.; Sekine, K.; Nagano, Y. Crack extension in hydraulic fracturing of shale cores using viscous oil, water, and liquid carbon dioxide. *Rock Mechanics and Rock Engineering* **2015**, *48* (4), 1463–1473.

(26) Li, X.; Feng, Z.; Han, G.; et al. Breakdown pressure and fracture surface morphology of hydraulic fracturing in shale with H<sub>2</sub>O, CO<sub>2</sub> and N<sub>2</sub>. *Geomech. Geophys. Geo-energ. Geo-resour.* **2016**, *2* (2), 63–76.

(27) Zhang, X.; Wang, J.; Gao, F.; Ju, Y. Impact of water, nitrogen and CO<sub>2</sub> fracturing fluids on fracturing initiation pressure and flow pattern in anisotropic shale reservoirs. *J. Nat. Gas Sci. Eng.* **2017**, *45*, 291–306.

(28) Wang, J.; Elsworth, D.; Wu, Y.; Liu, J.; Zhu, W.; Liu, Y. The influence of fracturing fluids on fracturing processes: a comparison between water, oil and SC-CO<sub>2</sub>. *Rock Mech. Rock Eng.* **2018**, *51*, 299–313.

(29) Zhang, C. P.; Cheng, P.; Ranjith, P. G.; Lu, Y. Y.; Zhou, J. P. A comparative study of fracture surface roughness and flow characteristics between CO<sub>2</sub> and water fracturing. *J. Nat. Gas Sci. Eng.* **2020**, *76*, 103188.

(30) Zhou, J.; Liu, G.; Jiang, Y.; Xian, X.; Liu, Q.; Zhang, D.; Tan, J. Supercritical carbon dioxide fracturing in shale and the coupled effects on the permeability of fractured shale: an experimental study. *J. Nat. Gas Sci. Eng.* **2016**, *36*, 369–377.

(31) Jia, Y.; Lu, Y.; et al. Surface characteristics and permeability enhancement of shale fractures due to water and supercritical carbon dioxide fracturing. *J. Pet. Sci. Eng.* **2018**, *165*, 284–297.

(32) Li, S.; Zhang, S.; Ma, X. Hydraulic Fractures Induced by Water-/Carbon Dioxide-Based Fluids in Tight Sandstones. *Rock Mech. Rock Eng.* **2019**, *52*, 3323–3340.

(33) Yang, B.; Haizhu, W.; Wang, B.; et al. Digital quantification of fracture in full-scale rock using micro-CT images: A fracturing experiment with N<sub>2</sub> and CO<sub>2</sub>. *J. Pet. Sci. Eng.* **2021**, *196*, 107682.

(34) Zhang, X.; Lu, Y.; Tang, J.; Zhou, Z.; Liao, Y. Experimental study on fracture initiation and propagation in shale using supercritical carbon dioxide fracturing. *Fuel* **2017**, *190*, 370–378.

(35) He, J.; Zhang, Y.; Yin, C.; Li, X. Hydraulic fracturing behavior in shale with water and supercritical CO<sub>2</sub> under triaxial compression. *Geofluids* **2020**, *2020*, 4918087.

(36) Zhao, Z.; Li, X.; He, J.; Mao, T.; Zheng, B.; Li, G. A laboratory investigation of fracture propagation induced by supercritical carbon dioxide fracturing in continental shale with interbeds. *J. Pet. Sci. Eng.* **2018**, *166*, 739–746.

(37) Hu, Y.; Liu, F.; Kang, Y.; Chen, H.; Liu, J. Propagation characteristics of supercritical carbon dioxide induced fractures under true tri-axial stresses. *Energies* **2019**, *12*, 4229.

(38) Zou, Y.; Li, N.; Ma, X.; Zhang, S.; Li, S. Experimental study on the growth behavior of supercritical CO<sub>2</sub>-induced fractures in a layered tight sandstone formation. *J. Nat. Gas Sci. Eng.* **2018**, *49*, 145–156.

(39) Xradia. *MicroXCT-200 and MicroXCT-400 User's Guide*, Version 7.0, revision 1.5 edition, 2010.

(40) Rodriguez, R.; Crandall, D.; Song, X.; Verba, C.; Soeder, D. Imaging techniques for analyzing shale pores and minerals: NETL-TRS-6–2014. *NETL Technical Report Series*; U.S. Department of Energy, National Energy Technology Laboratory: Morgantown, WV, 2014; p 40.

(41) Wang, H.; Lu, Q. Design of experimental system for supercritical CO<sub>2</sub> fracturing under confining pressure conditions. *J. Instrum.* **2018**, *13* (3), P03017.

(42) Wildenschild, D.; Sheppard, A. P. X-ray imaging and analysis techniques for quantifying pore-scale structure and processes in subsurface porous medium systems. *Adv. Water Resour.* **2013**, *51*, 217–246.

(43) Wang, L.; Yao, B.; et al. Experimental investigation of injection-induced fracturing during supercritical CO<sub>2</sub> sequestration. *Int. J. Greenhouse Gas Control* **2017**, *63*, 107–117.

(44) Hubbert, M. K.; Willis, D. G. Mechanics of Hydraulic Fracturing. *Trans. Soc. Pet. Eng.* **1957**, *210* (01), 153.

(45) Haimson, B.; Fairhurst, C. Initiation and extension of hydraulic fractures in rocks. *SPEJ, Soc. Pet. Eng. J.* **1967**, *7* (03), 310–318.

(46) Detournay, E. E.; Cheng, A. E. Influence of pressurization rate on the magnitude of the breakdown pressure. *The 33th US Symposium on Rock Mechanics (USRMS)*, Santa Fe, NM, June 3–5, 1992; American Rock Mechanics Association.

(47) Zoback, M. D. *Reservoir geomechanics*; Cambridge University Press: Cambridge, UK, 2010.

(48) Wang, Y.; Li, X.; He, J.; Zhao, Z.; Zheng, B. Investigation of fracturing network propagation in random naturally fractured and laminated block experiments. *Energies* **2016**, *9*, 588.

- (49) Chen, Y. Q.; Nagaya, Y.; Ishida, T. Observations of fractures induced by hydraulic fracturing in anisotropic granite. *Rock Mech Rock Eng.* **2015**, *48* (4), 1455–1461.
- (50) Liu, L. Y.; Zhu, W. C.; Wei, C. H.; Elsworth, D.; Wang, J. H. Microcrack based geomechanical modeling of rock-gas interaction during supercritical CO<sub>2</sub> fracturing. *J. Pet. Sci. Eng.* **2018**, *164*, 91–102.
- (51) Iassonov, P.; Gebrenegus, T.; Tuller, M. Segmentation of x-ray computed tomography images of porous materials: A crucial step for characterization and quantitative analysis of pore structures. *Water Resour. Res.* **2009**, *45* (9), W09415.
- (52) Arakawa, K.; Takahashi, K. Relationships between fracture parameters and fracture surface roughness of brittle polymers. *Int. J. Fract.* **1991**, *48* (2), 103–114.
- (53) Falconer, K. *Fractal geometry: mathematical foundations and applications*; John Wiley & Sons, 2004.
- (54) Peitgen, H.-O.; Jürgens, H.; Saupe, D. *Chaos and fractals: new frontiers of science*; Springer Science & Business Media, 2006.
- (55) Yan, Y.; Letscher, D.; Ju, T. Voxel cores: Efficient, robust, and provably good approximation of 3d medial axes. *ACM Transactions on Graphics (TOG)* **2018**, *37* (4), 1–13.
- (56) Bonnet, E.; Bour, O.; Odling, N. E.; Davy, P.; Main, I.; Cowie, P.; Berkowitz, B. Scaling of fracture systems in geological media. *Rev. Geophys.* **2001**, *39* (3), 347–383.
- (57) Taud, H.; Parrot, J.-F. Measurement of dem roughness using the local fractal dimension. *Géomorphologie: relief, processus, environnement* **2005**, *11* (4), 327–338.
- (58) Dutilleul, P.; Han, L.; Valladares, F.; Messier, C. Crown traits of coniferous trees and their relation to shade tolerance can differ with leaf type: a biophysical demonstration using computed tomography scanning data. *Front. Plant Sci.* **2015**, *6*, 172.
- (59) Reniers, D.; van Wijk, J.; Telea, A. Computing Multiscale Curve and Surface Skeletons of Genus 0 Shapes Using a Global Importance Measure. *IEEE Transactions on Visualization and Computer Graphics* **2008**, *14* (2), 355–368.
- (60) Gong, W.; Bertrand, G. A simple parallel 3D thinning algorithm. *Proceedings of the 10th International Conference on Pattern Recognition*, Atlantic City, NJ, June 16–21, 1990; IEEE Computer Society Press; pp 188–190..
- (61) Lee, T.-C.; Kashyap, R. L.; Chu, C. N. Building skeleton models via 3-D medial surface/axis thinning algorithms. *CVGIP: Graphical Models and Image Processing* **1994**, *56* (6), 462–478.
- (62) Lobregt, S.; Verbeek, P. W.; Groen, F. C. A. Three-dimensional skeletonization: Principle algorithm. *IEEE Trans. Pattern Anal. Mach. Intell.* **1980**, *2*, 75–77.
- (63) Pudney, C. Distance-ordered homotopic thinning: a skeletonization algorithm for 3D digital images. *Computer Vision and Image Understanding* **1998**, *72* (3), 404–413.
- (64) Dawei, Z.; Guangqing, Z.; Pengyun, Z.; et al. Effects of post-instability induced by supercritical CO<sub>2</sub> phase change on fracture dynamic propagation. *J. Pet. Sci. Eng.* **2018**, *162*, 358–366.